Mechanisms of Heat Content and Thermocline Change in the Subtropical and Subpolar North Atlantic

RICHARD G. WILLIAMS AND VASSIL ROUSSENOV

University of Liverpool, Liverpool, United Kingdom

M. SUSAN LOZIER

Duke University, Durham, North Carolina

DOUG SMITH

Met Office Hadley Centre, Exeter, United Kingdom

(Manuscript received 3 February 2015, in final form 16 September 2015)

ABSTRACT

In the North Atlantic, there are pronounced gyre-scale changes in ocean heat content on interannual-to-decadal time scales, which are associated with changes in both sea surface temperature and thermocline thickness; the subtropics are often warm with a thick thermocline when the subpolar gyre is cool with a thin thermocline, and vice versa. This climate variability is investigated using a semidiagnostic dynamical analysis of historical temperature and salinity data from 1962 to 2011 together with idealized isopycnic model experiments. On time scales of typically 5 yr, the tendencies in upper-ocean heat content are not simply explained by the area-averaged atmospheric forcing for each gyre but instead dominated by heat convergences associated with the meridional overturning circulation. In the subtropics, the most pronounced warming events are associated with an increased influx of tropical heat driven by stronger trade winds. In the subpolar gyre, the warming and cooling events are associated with changes in western boundary density, where increasing Labrador Sea density leads to an enhanced overturning and an influx of subtropical heat. Thus, upper-ocean heat content anomalies are formed in a different manner in the subtropical and subpolar gyres, with different components of the meridional overturning circulation probably excited by the local imprint of atmospheric forcing.

1. Introduction

There is a background warming of the North Atlantic (Levitus et al. 2012) revealed in the increase in ocean heat content and sea surface temperature over the basin in the last few decades (Fig. 1, right). The heat content anomalies often contain marked gyre contrasts over much of the record; the subtropics are usually warm when the subpolar gyre is cool and vice versa (Fig. 1a). These gyre-scale contrasts in ocean heat content are connected to different atmospheric states (Lozier et al. 2008) as well as to differences in meridional overturning circulation (Lozier et al. 2010) and associated heat convergence (Williams et al. 2014).

While these connections have been previously discussed, what remains unclear is why gyre-scale contrasts are more evident in the anomaly patterns for ocean heat content than for sea surface temperature (Figs. 1a,b). The physical mechanisms leading to the pronounced gyre-scale contrasts in ocean heat content anomalies are explored here. Ocean heat content is altered by changes in local atmospheric forcing; air–sea fluxes alter sea surface temperature, and wind-induced upwelling alters the vertical position of isotherms.

Denotes Open Access content.

Corresponding author address: Richard G. Williams, Department of Earth, Ocean and Ecological Sciences, School of Environmental Sciences, University of Liverpool, 4 Brownlow Hill, Liverpool L69 3GP, United Kingdom.
E-mail: ric@liv.ac.uk

DOI: 10.1175/JCLI-D-15-0097.1

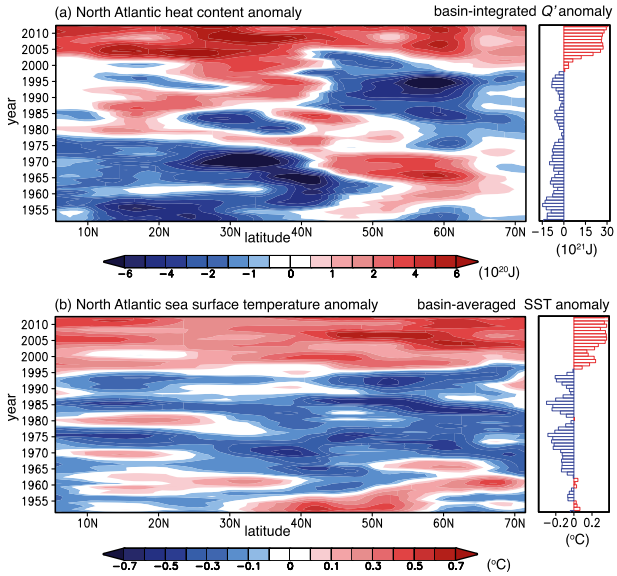

FIG. 1. (left) Hovmöller plots for North Atlantic anomalies from 1950 to 2013: (a) zonally and full-depth-integrated heat content over 1° meridional bins given by $\overline{Q'}^{x}(t, y)$ (10^{20} J) and (b) zonally averaged sea surface temperature (°C). (right) The basin-integrated heat content anomaly in (a) and the basin-averaged sea surface temperature in (b). Data diagnostics from the Met Office hydrographic dataset and a 3-yr running mean is applied.

Ocean heat content also changes as a result of the convergence of ocean heat transport, which itself is altered by local or remote changes in atmospheric forcing and dynamical circulation.

In terms of the underlying physical mechanisms, the change in sign in the heat content anomalies between the subtropical and subpolar gyres (Fig. 1a) provides an important clue as to their formation. Classical gyre theory explains how the large-scale North Atlantic wind pattern drives subtropical and subpolar gyre circulations (Luyten et al. 1983), with the subtropical gyre characterized by downwelling, deepening isotherms and a sharp thermocline (a region of enhanced vertical temperature gradient) and the subpolar gyre characterized by upwelling, a shoaling of the isotherms, and a thin or outcropping thermocline.

In this study, the relationship between upper-ocean heat content and thermocline anomalies is explored using historical temperature and salinity data in the North Atlantic (section 2). The evolution of the heat anomalies are then compared with air–sea heat flux reanalyses and our diagnostics for the heat convergence for each gyre (section 3), exploiting a semi-diagnostic analysis of historical temperature and salinity data and modifying our prior study (Williams et al. 2014) by using ECMWF, rather than NCEP, winds. Extending our prior analyses, the mechanisms controlling the heat convergences for each gyre are identified, particularly revealing the importance of the meridional overturning and associated heat transport on the gyre boundaries (section 4). The controlling mechanisms are illustrated via idealized double-gyre model experiments (section 5), and, finally, the wider implications are discussed (section 6).

2. Historical heat content and thermocline changes

The connection between heat content anomalies, sea surface temperature, and thermocline thickness are now explored using analyses of historical temperature and salinity data.

a. *Evaluation of heat content*

The historical temperature and salinity changes are derived from a global analysis of the available hydrographic data and recent Argo data from 1950 to 2011 (Met Office statistical ocean reanalysis; Smith et al. 2015). The analysis fills data sparse regions by extrapolating from the observational data using covariances from the Hadley Centre model, which are iteratively updated using repeat model ensemble integrations with perturbed physics (Smith et al. 2010). The Hadley Centre analyses are on a 1.25° grid with 20 vertical levels and are linearly interpolated onto a 1° grid with 23 vertical levels over the globe.

The local heat content anomaly per unit horizontal area (joules per meter squared) is defined as follows:

$$Q'(x,y,t) = \rho_0 C_p \int_{-D}^{0} \theta'(x,y,z,t)\, dz, \qquad (1)$$

where θ is the potential temperature, the prime denotes a temporal deviation from a time mean, D is either taken as the full ocean depth or as a fixed horizon of 1300 m for the upper ocean, ρ_0 and C_p are the reference density and heat capacity, respectively, and their product is taken as a constant of $4.09 \times 10^6\,\mathrm{J\,K^{-1}m^{-3}}$ from a basin average. The heat content anomaly for a domain (joules) is then evaluated as an area integral, denoted by the overbar with superscripts x, y: $\overline{Q'}^{x,y}(t) \equiv \int_A Q'(x, y, t)\, dA$, where A is the horizontal extent of the domain.

b. *Evolution of anomalies in heat content, sea surface temperature, and depth of potential density surfaces*

The full-depth ocean heat content anomaly $\overline{Q'}^{x,y}(t)$ reveals different responses over the subtropical and subpolar regions of the North Atlantic; the subtropics are anomalously cool from 1950 to the mid-1970s and

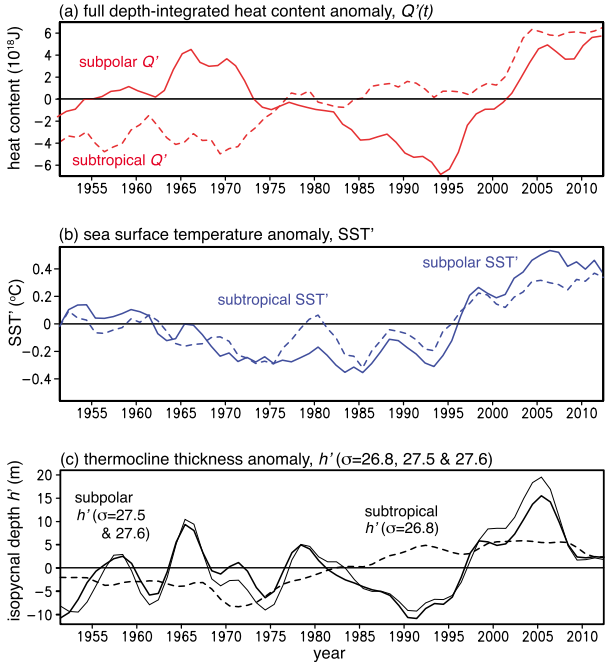

FIG. 2. Time series of gyre-scale climate anomalies: (a) full-depth-integrated heat content $\overline{Q'}^{x,y}$ (10^{18} J; red lines) averaged over the subtropics (5°–46°N; dashed) and the subpolar gyre (46°–75°N; solid), (b) SST (°C; blue lines), and (c) depth of potential density surfaces h' (m; black lines) taken as $\sigma = 26.8$ for the subtropics and $\sigma = 27.5$ and 27.6 (thin line) for the subpolar gyre (time-mean depths of 330, 360, and 470 m, respectively). A 3-yr running mean is applied.

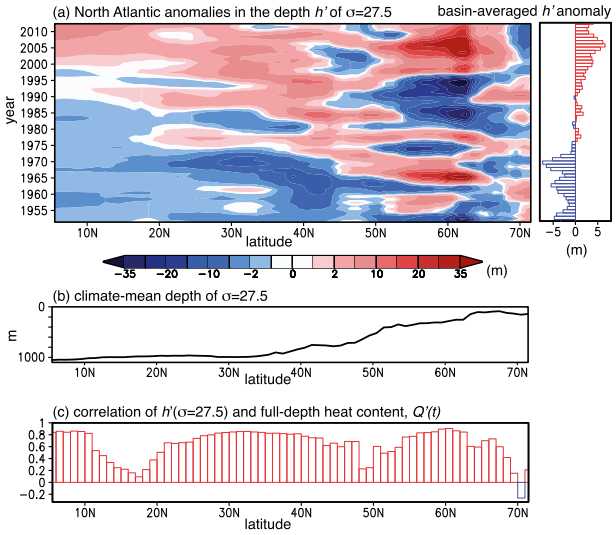

FIG. 3. (a) Hovmöller plot for the zonally averaged anomaly of the depth of the $\sigma = 27.5$ surface h' (m) taken to be representative of depth anomalies of the thermocline (a positive anomaly represents a deeper surface), with the basin-averaged depth at right; (b) climate-mean depth of $\sigma = 27.5$ surface (m) taken from annual-mean analyses; and (c) the correlation between the zonally averaged depth of the $\sigma = 27.5$ surface and the zonally integrated full-depth heat content (as in Fig. 1a) for 1951–2012. A 3-yr running mean is applied.

then warm from 2000 to 2011 (Fig. 2a, dashed line), while the subpolar gyre is anomalously warm in the mid-1960s, cool in the mid-1990s, and again warm from 2003 onward (Fig. 2a, solid line). In contrast, the sea surface temperature reveals subtropical and subpolar anomalies that are broadly similar to each other (Fig. 2b), with warm anomalies suggested in the mid-1950s, cool anomalies in the mid-1970s and 1980s, and warmer anomalies since 1995 (Fig. 1b).

There are also changes in the depth of potential density surfaces across the basin, illustrated here using area averages for $\sigma = 26.8$ for the subtropics and $\sigma = 27.5$ and 27.6 for the subpolar gyre (Fig. 2c); their time-mean depths are 330 m in the subtropics and 360 and 470 m in the subpolar gyre, respectively, so that these surfaces reside in the upper thermocline and outcrop during winter. In the subtropics, the $\sigma = 26.8$ surface generally changes from being anomalously shallow (a negative anomaly) in the 1960s to being deep (a positive anomaly) from the mid-1990s onward (Fig. 2c, dashed line). In the subpolar gyre, the $\sigma = 27.5$ and 27.6 surfaces instead vary from being anomalously deep in the mid-1960s, to shallow in the 1990s, and back to deep again in 2005 (Fig. 2c, solid lines). Thus, the depth changes of these potential density surfaces in the subtropical and subpolar gyres often have opposing signs but then are in phase with each other from 1997 to the end of the record.

In summary, subtropical and subpolar gyre contrasts are revealed in ocean heat content anomalies but are less apparent in sea surface temperature anomalies. These gyre contrasts in heat content anomalies might then result from changes in the vertical displacement of potential density surfaces.

c. *Evolution of heat content and thermocline anomalies*

Pursuing the link between ocean heat content and upper density structure further, there are often gyre contrasts in the depth of the same σ surface over the basin (Figs. 3a,b for $\sigma = 27.5$). These depth anomalies in σ surfaces are strongly correlated with the full-depth zonally integrated ocean heat content over much of the basin (Fig. 3c; correlation coefficient $r \sim 0.8$), except close to gyre boundaries at 15° and 48°N.

This connection between the depth of σ surfaces and heat content anomalies reflects the strong control of the thermocline on ocean heat content; a deeper thermocline corresponds to deeper σ surfaces, a greater extent of warm water, and a larger heat content. In turn, the thermocline is understood to be deep over the subtropics

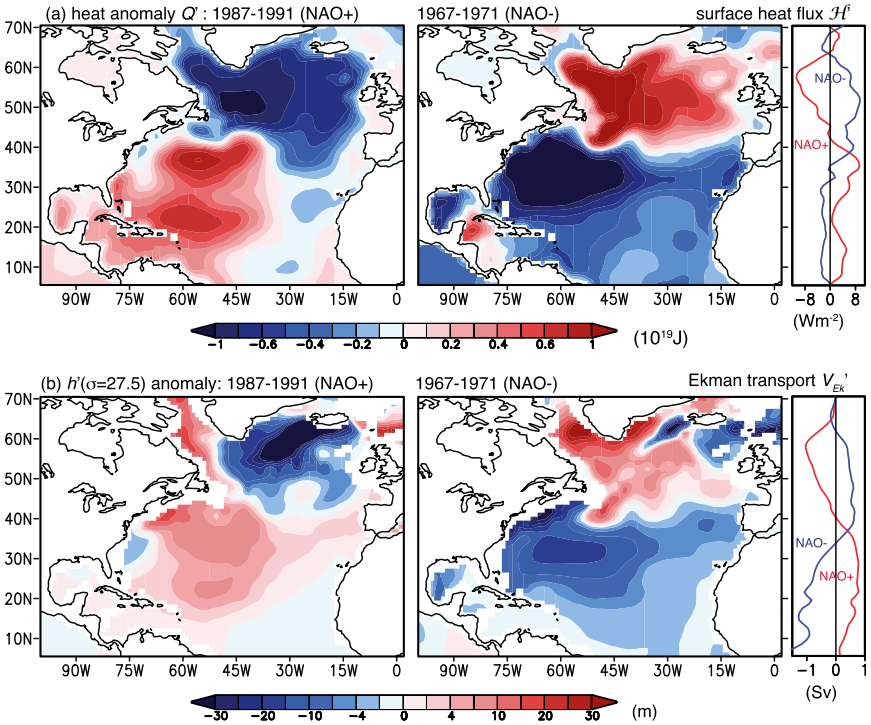

FIG. 4. Anomaly maps for two different states of atmospheric forcing: (left) NAO+ for 1987–91 and (center) NAO− for 1967–71: (a) full-depth-integrated heat content anomaly $Q'(x, y)$ (10^{19} J) with (right) surface heat flux anomaly into the ocean $\mathcal{H}'$ (W m^{-2}, zonally averaged) and (b) thermocline depth anomaly, using depth anomalies of $\sigma = 27.5$ surface to represent undulations of the thermocline and (right) northward surface Ekman transport V'_{Ek} (Sv; 1 Sv $\equiv$ 10^6 m^3 s^{-1}). Anomalies are defined relative to a time-mean from 1950 to 2013.

as a result of wind-induced downwelling and thin over the equator and subpolar gyre as a result of wind-induced upwelling (Luyten et al. 1983). Thus, changes in atmospheric forcing and circulation are likely to alter the thermocline, the depth of σ surfaces, and heat content.

The link to different states of atmospheric forcing is illustrated here for two opposing phases of the winter North Atlantic Oscillation (NAO) index (Hurrell 1995): for a positive NAO phase (NAO+) period from 1987 to 1991, there is an anomalously warm subtropics and a cool subpolar gyre, while for a negative NAO phase (NAO−) period from 1967 to 1971, there is instead an anomalously cool subtropics and a warm subpolar gyre (Fig. 4a; also see Lozier et al. 2008). The sign of the heat content anomalies is consistent with their formation by the zonally averaged air–sea heat fluxes (Fig. 4a, right); this causal connection is explored later. The depth anomalies of the $\sigma = 27.5$ surface are taken to be representative of changes in the depth of the thermocline and reveal a sharp subtropical–subpolar contrast (Fig. 4b); for NAO+, the thermocline is anomalously deep in the subtropics and shallow in the subpolar gyre, while for the NAO− period, the thermocline is anomalously shallow in the subtropics and deep in the subpolar gyre. Changes in the subtropical thermocline are related to changes in Ekman transport over the basin (Fig. 4b, right); for example, a deep or shallow thermocline coincides, respectively, with enhanced or reduced northward Ekman transport from the tropics. Thus, the sign of the heat content anomalies are consistent with both the anomalies in air–sea heat fluxes and Ekman transport.

TABLE 1. Correlations between area-averaged anomalies of full-depth ocean heat content Q', SST′, and depth of $\sigma = 27.5$ surface h' for the North Atlantic (0°–75°N), the tropics–subtropics (5°–46°N), and subpolar (46°–75°N) from 1961 to 2012. Correlations are evaluated after the time series are detrended and a 3-yr running mean is applied. Confidence limits are estimated using a Monte Carlo approach (Wilks 1995); correlations displayed in boldface if greater than ±0.49 (99% confidence limit), lightface if greater than ±0.32 (90% confidence limit), and otherwise in italic.

Correlation	Basin	Subtropical	Subpolar
Q', SST′	**0.70**	**0.54**	**0.62**
Q', h' ($\sigma = 27.5$)	0.34	**0.54**	**0.71**
SST′, h' ($\sigma = 27.5$)	0.35	*0.12*	**0.53**

In summary, the basin-scale rise in heat content is connected to the rise in sea surface temperature and increase in thermocline thickness (Figs. 1a,b and 3a, right; Table 1), while the contrasts in subtropical and subpolar heat content are affected by the similarly signed contrasts in thermocline thickness (Fig. 3c).

3. Formation of gyre-scale heat anomalies

The aim is now to explore whether the gyre-scale heat content and associated thermocline anomalies are explained by the atmospheric forcing and/or the convergences in heat transport over each gyre.

a. Upper-ocean heat budget

The evolution of the local heat anomaly Q' (joules per meter squared) from a depth integral of the potential temperature from the sea surface to a horizon D is controlled by the temporal anomalies in the air–sea heat flux $\mathcal{H}_s'$ and the convergence of the advective heat flux:

$$\frac{\partial Q'}{\partial t} \equiv \rho_0 C_p \int_{-D}^{0} \frac{\partial \theta'}{\partial t} dz = \mathcal{H}_s' - \rho_0 C_p \int_{-D}^{0} \nabla \cdot (\mathbf{u}\theta)' \, dz, \tag{2}$$

where $\mathbf{u}$ is the three-dimensional velocity and the effects of diffusive and convective transfers are ignored (with convection assumed to be shallower than D, taken henceforth as 1300 m). Integrating (2) over the domain, from west to east boundaries, and meridionally from the southern to northern boundaries (from y_s to y_n) the evolution of the area-integrated heat anomaly $\overline{Q'}^{x,y}$ (joules) is given by

$$\frac{\partial \overline{Q'}^{x,y}}{\partial t} = \overline{\mathcal{H}_s'}^{x,y} - \rho_0 C_p \left\{ \left[\int_{-D}^{0} \overline{(v\theta)'}^{x} dz \right]_{y_s}^{y_n} + \overline{(w\theta)'}^{x,y} \Big|_{-D} \right\}, \tag{3}$$

where the overbar with superscript x represents a west–east integral over the domain given by $\overline{(v\theta)}^{x} \equiv \int v\theta \, dx$ and with superscripts x, y represents an area average given by $\overline{(w\theta)}^{x,y} \equiv \int w\theta \, dA$, v is the meridional velocity, and w is the vertical velocity. Hence, the tendency in area-integrated upper-ocean heat content $\partial \overline{Q'}^{x,y}(t)/\partial t$ is given by the area-integrated air–sea heat flux anomaly plus the sum of the convergence in northward upper-ocean heat transport anomaly through the meridional boundaries and the vertical heat advection anomaly at depth D [first, second, and third terms on rhs of (3), respectively].

The time series for the heat content tendency, air–sea heat flux, and heat convergences in (3) are subsequently compared with each other. To identify confidence levels for the correlations after temporal smoothing, a Monte Carlo approach (Wilks 1995) is applied: 2000 pairs of time series of random numbers are generated with the same length as the annual datasets; after a temporal smoothing of 5 yr, correlations for each pair are calculated and the absolute values of the correlations are sorted in ascending order; and then the level of significance is given by the maximum correlation for that proportion of random pairs, such that a 95% limit corresponds to the correlation value for 1900 random pairs from the full set of 2000 pairs.

b. Connection between gyre-scale heat content anomalies and air–sea heat fluxes

Based on a simplified local heat balance, $\partial \overline{Q'}^{x,y}(t)/\partial t$ follows the air–sea heat flux anomaly $\overline{\mathcal{H}_s'}^{x,y}(t)$ integrated over each gyre:

$$\frac{\partial \overline{Q'}^{x,y}}{\partial t} \sim \overline{\mathcal{H}_s'}^{x,y}. \tag{4}$$

To assess this local relationship (4), the tendency of the heat content anomaly is evaluated over the upper ocean (from the surface to a depth of 1300 m) and from 1962 to 2011 (to avoid the large errors arising from deeper temperature anomalies and the earlier part of the record). The air–sea heat flux $\mathcal{H}_s$ is taken either from ECMWF, using a combination of ERA-40 and ERA-Interim (the latter from 1979 onward), or from NCEP (Figs. 5a,b, red and blue lines, respectively); see Josey et al. (2013) for a discussion of different air–sea flux datasets. The time series are compared after a 5-yr running average is applied. Integrated over the tropics–subtropics from 5° to 46°N, $\partial \overline{Q'}^{x,y}/\partial t$ is sometimes the same sign as $\overline{\mathcal{H}_s'}^{x,y}$, although the correlation coefficients are relatively low (Table 2). Over the subpolar gyre, $\partial \overline{Q'}^{x,y}/\partial t$ does not relate to $\overline{\mathcal{H}_s'}^{x,y}$ (Fig. 5b); there is no significant correlation with either of the reanalyses (Table 2).

Hence, the evolution of the gyre-scale heat content anomalies on a 5-yr time scale is not convincingly explained by the area-integrated air–sea heat flux anomalies. Given this difficulty of explaining the subtropical and subpolar anomalies through purely a local response, the effects of heat transport across the boundaries of each gyre are next considered.

c. Dynamical assimilation of historical temperature and salinity data

To estimate the heat convergence (3), the historical temperature and salinity data are assimilated into a dynamical model in a semidiagnostic manner (Williams

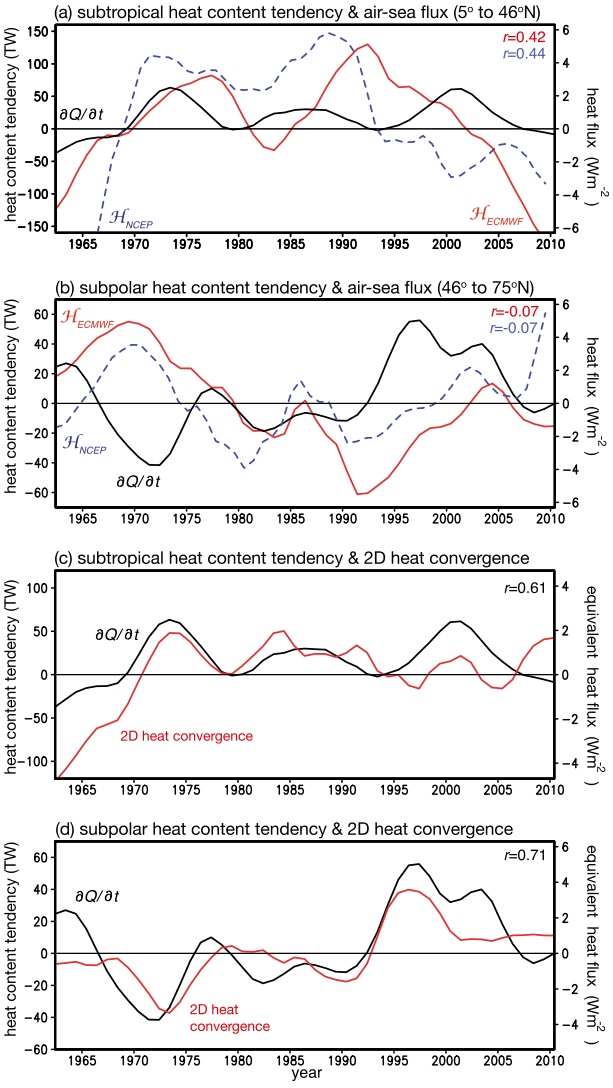

FIG. 5. Time series of anomalies in $\partial\overline{Q^r}^{x,y}/\partial t$ (TW; black line) evaluated over the upper 1300 m with (a),(b) $\overline{\mathcal{H}_s^r}^{x,y}$ (W m^{-2}) based on an area integral of ECMWF (ERA-40 and ERA-Interim; red lines) and NCEP (updated reanalysis in 2014; blue dashed lines) fluxes and with (c),(d) the horizontal and vertical heat convergence anomalies (TW; red line) over the upper 1300 m. The diagnostics are applied in (a) and (c) for the tropics and subtropics (5°–46°N) and in (b) and (d) for the subpolar regions (46°–75°N) from 1962 to 2010; the left-hand y axis is the area-integrated heat uptake (TW), and the right-hand y axis is the equivalent surface heat flux into the ocean (W m^{-2}). A 5-yr running mean is applied.

et al. 2014) [following Mellor et al. (1982) and Greatbatch et al. (1991)]:

(i) The Massachusetts Institute of Technology (MIT) general circulation model (Marshall et al. 1997) is initialized with the Hadley Centre analyses of temperature and salinity data (Smith and Murphy 2007), interpolating the slightly coarser historical data analyses onto a 1° grid with 23 vertical levels over the globe.

TABLE 2. Correlations of $\partial\overline{Q^r}^{x,y}/\partial t$ (0–1300 m) and heat transport convergence (0–1300 m) for the subtropics and subpolar latitudes and air–sea heat flux from 1962 to 2009 for air–sea heat fluxes alone, for the 2D heat convergence alone, and for the 2D convergence with the air–sea heat flux included. Air–sea fluxes are taken from either ECMWF (combination of ERA-40 and ERA-Interim) or NCEP (updated reanalysis in 2014). Time series are detrended and a 5-yr running mean is applied. Confidence limits with a running mean applied are estimated using a Monte Carlo approach (Wilks 1995): correlations are shown in boldface if greater than ±0.61 (99% confidence limit), lightface if greater than ±0.51 (95% confidence limit), and otherwise in italic.

Correlation of $\partial\overline{Q^r}^{x,y}/\partial t$	Subtropical	Subpolar
ECMWF $\overline{\mathcal{H}_s^r}^{x,y}$	*0.42*	*−0.07*
NCEP $\overline{\mathcal{H}_s^r}^{x,y}$	*0.44*	*−0.07*
2D convergence of heat transport	**0.61**	**0.71**
2D convergence of heat transport and ECMWF $\overline{\mathcal{H}_s^r}^{x,y}$	0.57	*0.33*
2D convergence of heat transport and NCEP $\overline{\mathcal{H}_s^r}^{x,y}$	*0.49*	*0.36*

(ii) This model assimilation includes an initial 1-month spinup and then a further 12-month integration to cover an annual cycle. The model includes forcing from monthly mean wind stresses from ECMWF for each year, rather than from NCEP as originally applied in Williams et al. (2014). The dynamical adjustment does not include explicit surface heat or freshwater fluxes but includes a weak artificial relaxation of temperature and salinity to the initial annually averaged temperature and salinity data on a time scale of 36 months, which acts to minimize model drift.

(iii) This initialization and assimilation procedure is repeated for each separate year. The subsequent changes in heat content and heat transport are then evaluated from these dynamically adjusted velocities and temperatures for each year.

Our approach ignores dynamical contributions from finer-scale circulations, such as mesoscale eddies and fronts, as well as any effects from seasonal variability in the hydrography.

d. *Heat convergence for the subtropical and subpolar gyres*

The evolution of the heat content anomalies is now compared with the convergence in horizontal and vertical heat transport over the upper 1300 m:

$$\frac{\partial\overline{Q^r}^{x,y}}{\partial t} \sim -\rho_0 C_p \left\{ \left[\int_{-D}^{0} \overline{(v\,\theta)^r}^{x}\, dz \right]_{y_s}^{y_n} + \overline{(w\,\theta)^r}^{x,y}\Big|_{-D} \right\}. \tag{5}$$

The time series are again averaged with a 5-yr running mean.

The heat convergence over the upper 1300 m of the subtropical gyre drives a heat content gain around 1975, in the mid-1980s, and possibly in 2000 (Fig. 5c, red line). There is reasonable agreement between the diagnosed tendency in upper-ocean heat content and the convergence in upper-ocean heat transport (Fig. 5c, red and black lines; correlation of $r = 0.61$ in Table 2). There are, however, some periods of mismatch, such as in the early part of the record from 1965 to 1970 when the heat convergence implies a large loss of heat and from 2007 to 2011 when the heat convergence instead implies a gain of heat. If the subtropical analysis is repeated over the full depth, the heat content tendency and heat convergence is only weakly correlated ($r = 0.35$), suggesting larger errors in reconstructing the heat balance at depth.

In the subpolar gyre, the upper-ocean thermal anomaly changes from positive to negative and back to positive over the period from 1955 to 2010 (Fig. 2a, solid line). The tendency of the upper-ocean heat content for the subpolar gyre broadly follows the convergence of heat transport over the subpolar gyre (Fig. 5d, red and black lines; $r = 0.71$ in Table 2). If the subpolar analysis is repeated over the full depth, the heat content tendency and heat convergence remains significantly correlated over the subpolar gyre ($r = 0.8$). Hence, the heat convergence is the primary driver of subpolar heat content changes, rather than the direct effect of air–sea heat fluxes.

4. Physical mechanisms controlling the heat convergence for each gyre

To gain insight into the mechanisms controlling the evolution of the heat content anomalies in each gyre, the heat convergence (5) is separated into different contributions in terms of different overturning and gyre contributions, evaluated over different depth ranges (0–100 m, 100–1300 m, etc.):

$$\rho_0 C_P \int_{-D}^{0} \overline{v\theta}^x \, dz = \rho_0 C_P \int_{-D}^{0} (\overline{v}^x \overline{\theta}^x + \overline{v^\dagger \theta^\dagger}^x) \, dz, \quad (6)$$

where the heat transport from the vertical cell is referred to as that from the meridional overturning circulation (MOC) and that from the horizontal cell as the gyre contribution (first and second terms on rhs); the superscript † represents a horizontal departure from a zonal integral for the velocity and a horizontal departure from a zonal mean for the potential temperature.

For the climate mean, the northward heat transport is dominated by the MOC contribution over the upper 100 m over the tropics (Fig. 6, green line) and the MOC contribution from 100 to 1300 m over the middle and high latitudes (Fig. 6, blue line), with a comparable gyre contribution over the high latitudes (Fig. 6, red line). This variation is similar to our previous mass-conserving decomposition for the heat transport, where the northward heat transport is carried by an Ekman cell in the low latitudes and a MOC-minus-Ekman cell in the middle and high latitudes and augmented by the gyre contribution at high latitudes (Williams et al. 2014). Given the different heat transport mechanisms dominating at different latitude ranges in the climate mean, we naturally suspect that the temporal variations in the subtropical and subpolar heat convergences (Figs. 5c,d) are achieved in a different manner in each gyre.

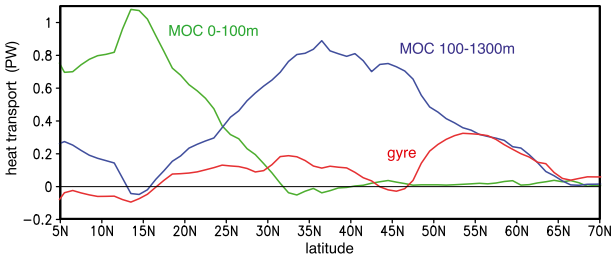

FIG. 6. Climate-mean, northward heat transport components (PW) vs latitude: MOC from 0 to 100 m (green) and from 100 to 1300 m (blue) and gyre (red) components. Evaluated over the upper 1300 m and based on a dynamical assimilation of densities repeated for each year 1962–2010.

a. *Heat convergence in the subtropical gyre*

The changes in heat convergence over the subtropical gyre involve partly opposing contributions in the heat convergence over the upper 100 m (Fig. 7a, green line) and the heat convergence from 100 to 1300 m (Fig. 7a, blue line), while the vertical heat advection at 1300 m is relatively small. The more pronounced changes in heat convergence generally follow the heat convergence over the upper 100 m. The heat convergence over the upper 100 m is dominated by the MOC contribution rather than the gyre contribution using (6) (Fig. 7b, green and purple lines).

This heat convergence over the upper 100 m is dominated by the heat transport anomalies on the southern boundary of the subtropics (nominally taken at 5°N) rather than those on the northern boundary at 46°N (Fig. 7c). On the southern boundary, the northward heat transport changes from a negative anomaly in 1965 to positive anomalies in 1975 and 2000 (Fig. 7c, red line), closely following the sign of the Ekman volume transport anomaly inferred from the wind stress (Fig. 7c, blue line).

In summary, the winds provide an important contribution to the MOC-related heat transport and convergence

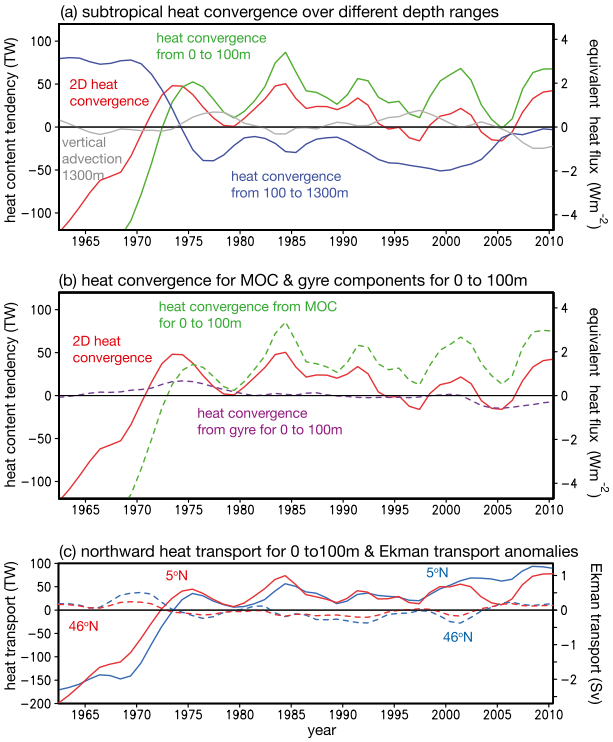

FIG. 7. Time series for subtropical heat convergence: (a) the 2D heat convergence anomalies (TW; red line) over the upper 1300 m separated into horizontal convergence over the upper 100 m (green line) and from 100 to 1300 m (blue line) and the vertical heat transport anomaly at 1300 m (gray line), and (b) horizontal convergence of heat transport anomaly over the upper 100 m separated into MOC (dashed green line) and gyre (dashed purple line) components. (c) Time series of anomalies in northward heat transport (TW; red lines) over the upper 100 m and northward Ekman volume transport diagnosed from the wind stress (Sv; blue lines) at the boundaries of the subtropical domain at 5° (solid lines) and 46°N (dashed lines). A 5-yr running mean is applied.

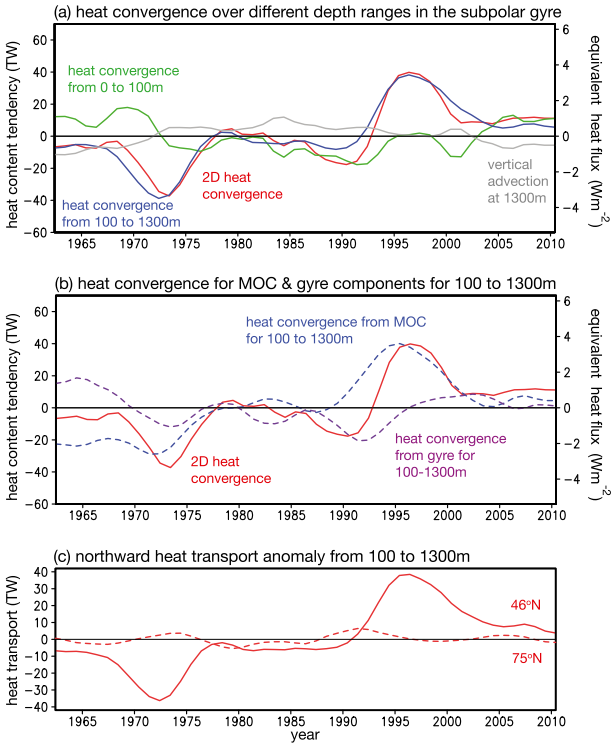

FIG. 8. Time series for subpolar heat convergence: (a) the 2D heat convergence anomalies (TW; red line) over the upper 1300 m separated into horizontal convergence over the upper 100 m (green line) and from 100 to 1300 m (blue line) and the vertical heat transport anomaly at 1300 m (gray line), (b) heat convergence from 100 to 1300 m separated into MOC (blue dashed line) and gyre (purple dashed line) components, and (c) northward heat transport (TW) from 100 to 1300 m through the subpolar boundaries at 46° (solid line) and 75°N (dashed line). A 5-yr running mean is applied.

over the subtropical gyre via the Ekman volume and heat transport; northward Ekman transports are driven by the trade winds and southward Ekman transports by the westerlies. The low-latitude changes in heat transport are particularly sensitive to the effect of the winds, with a fixed change in wind stress leading to a relatively large change in Ekman volume flux through the smallness of the Coriolis parameter at low latitudes.

b. Heat convergence in the subpolar gyre

The mechanisms controlling the heat content cycle in the subpolar gyre are different from those in the subtropics. The changes in the heat convergence over the subpolar gyre are generally dominated by the heat convergence from 100 to 1300 m (Fig. 8a, blue line) rather than by the heat convergence over the upper 100 m or the vertical heat advection at 1300 m. The heat convergence from 100 to 1300 m is affected both by the heat convergence from the MOC and by the horizontal, gyre contributions (Fig. 8b, blue and purple lines).

The changes in the subpolar convergence in heat from 100 to 1300 m are primarily a result of larger changes in heat transport at the subtropical–subpolar boundary at 46°N rather than relatively small changes at 75°N (Fig. 8c). The heat transport anomalies from 100 to 1300 m at 46°N mainly reflect changes in the MOC over that depth range. The MOC from 100 to 1300 m at 46°N is itself positively correlated with the density content in the western Labrador Sea (Figs. 9a,b; $r = 0.88$ with zero lag), where the density content (from the depth integral of density) is evaluated at depths greater than 300 m and west of 58°W. In turn, the density content for the western Labrador Sea slightly lags the heat content over the entire Labrador Sea with a slight

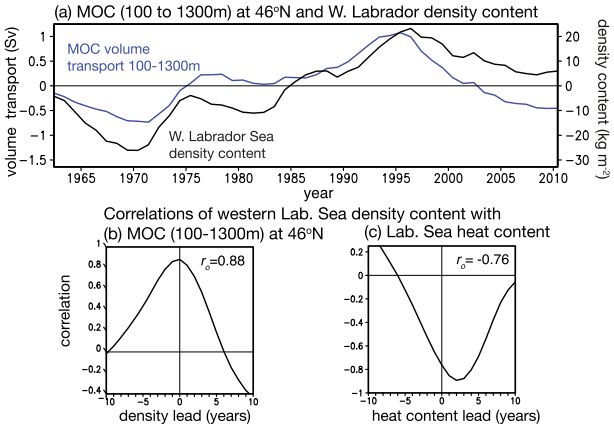

FIG. 9. (a) Time series of MOC from 100 to 1300 m (Sv; blue line) at 46°N and western Labrador Sea density content from a depth integral of density (kg m^{-2}; black line) west of 55°W; time-lagged correlation between detrended time series for the western Labrador Sea density content with (b) the MOC from 100 to 1300 m at 46°N and (c) the heat content over the entire Labrador Sea (r_0 is the correlation at zero lag). A 5-yr running mean is applied.

delay of 2 yr (Fig. 9c; $r = -0.76$ at zero lag) owing to communication to the boundary. In our view, the density changes in the western Labrador Sea are likely to be communicated along the western boundary, via a combination of advection and boundary wave propagation (Hughes and Meredith 2006; Roussenov et al. 2008), and then lead to meridional overturning changes via thermal-wind balance at the intergyre boundary (Marotzke et al. 1999; Bingham and Hughes 2008).

The Labrador Sea heat content anomaly itself positively correlates with the local air–sea heat flux into the ocean, and the depth of isopycnals positively correlates with the Ekman downwelling (correlation coefficient $r = 0.78$ and 0.81, respectively, between detrended time series). However, unraveling the separate contributions of the air–sea heat flux and Ekman downwelling is difficult, as they covary (correlation coefficient $r = 0.73$).

Indeed, Straneo (2006) demonstrates that density changes in the western boundary at the exit of the Labrador Sea are a complex result of local air–sea buoyancy forcing and local dynamics, involving the strength and properties of the wind-driven boundary current that rims the basin interior and, importantly, the strength of the eddies that exchange heat and salt between the interior and the boundary current waters. Thus, the primary mechanism driving these density anomalies may vary in time as the wind and buoyancy forcing vary in amplitude, and their effects may be modulated by the local dynamics.

A caveat is that our subpolar heat budget is applied over the upper 1300 m and does not account for winter convection extending to greater depths, which can sometimes occur in the Labrador and Irminger Sea basins (Yashayaev 2007; Pickart et al. 2003). However, our inference of heat convergence controlling the subpolar heat content evolution still holds when the analysis is repeated over the full ocean depth (Williams et al. 2014). Our inference of a relatively weak direct effect of air–sea heat fluxes for the gyre-scale heat content is, however, based on applying running time means of 5 yr. Annual air–sea heat fluxes might possibly provide a more comparable contribution to advective heat convergence on shorter interannual time scales in the subpolar gyre (Grist et al. 2010).

Our conclusion that heat tendency over the subpolar gyre is controlled by heat convergence is also suggested by coupled atmosphere–ocean model studies of two events. The cooling of the subpolar gyre in the early 1970s (Fig. 8b) is achieved by a reduction in overturning and heat convergence (Robson et al. 2014b), which is preceded by a high Labrador Sea heat content (Figs. 9a,c). Conversely, the dramatic warming of the subpolar gyre in the mid-1990s (Fig. 8b) is achieved by an increased overturning (Robson et al. 2012) and convergence in the heat transport (Fig. 8b), which is preceded by a low Labrador Sea heat content (Figs. 9a,c).

In summary, the heat content tendency of the subpolar gyre is not directly connected to atmospheric forcing on time scales of typically 5 yr. Instead, changes in the western boundary density, resulting from a combination of air–sea forcing and local dynamics, alter the meridional overturning at the intergyre boundary and control the heat convergence over the subpolar gyre. Air–sea forcing may be significant, however, on a more regional basis and on shorter interannual time scales.

5. Idealized model illustration of heat content controls

The different mechanisms affecting ocean heat content for each gyre are now further investigated via two sets of idealized model experiments using a layered isopycnal model configured for an ocean basin. The model experiments employ an isopycnic model [Miami Isopycnic Coordinate Ocean Model (MICOM), version 2.7 (Bleck and Smith 1990), using a formulation similar to Roussenov et al. (2008)]. The model domain extends from 30°S to 65°N and from 76° to 8°W with a flat bottom and employs a horizontal resolution of 1.4° on a Mercator grid and 12 σ_0 isopycnal layers in the vertical plus a surface mixed layer with variable density. At the southern

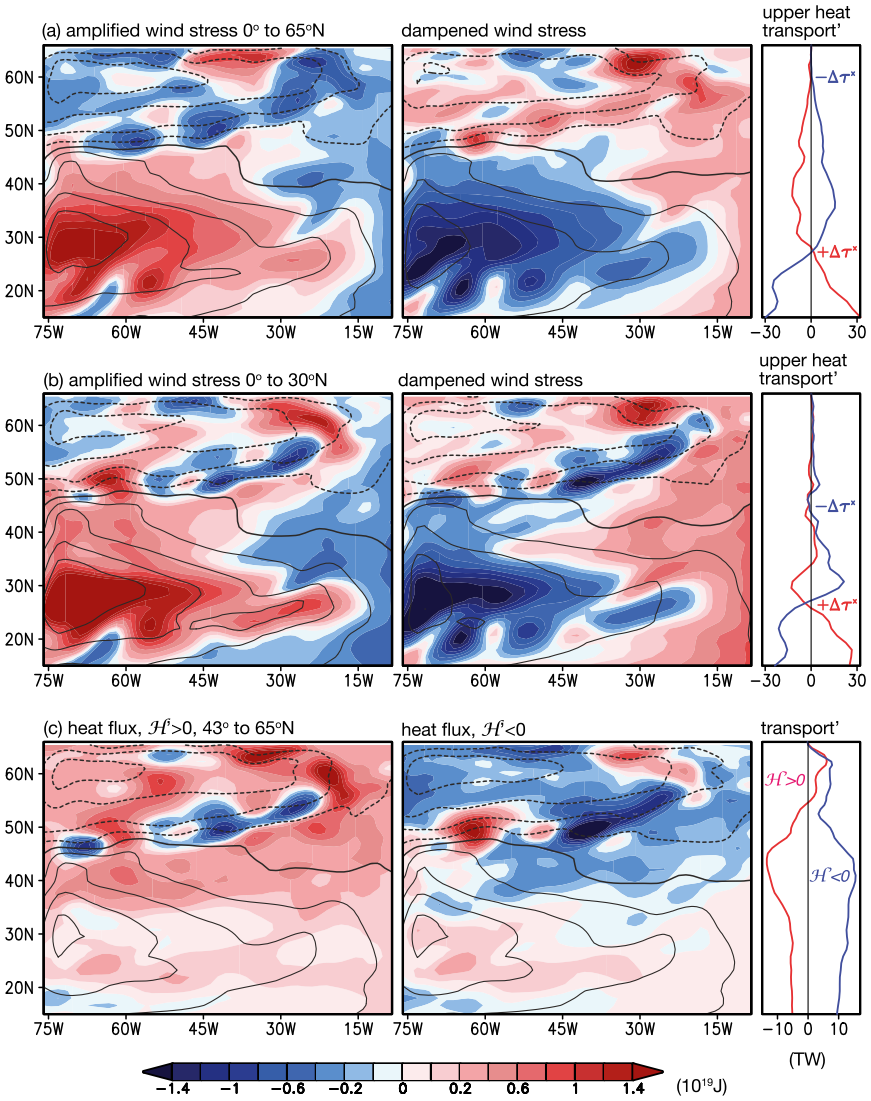

FIG. 10. Ocean model experiments for a double gyre in an idealized rectangular basin. Full-depth heat content anomaly (10^{19} J) for separate perturbations in atmospheric forcings after five years: (a) wind stress amplified by a factor of (left) 1.25 or (center) 0.75 over the entire basin, (b) as in (a), but restricted to low latitudes up to 30°N, and (c) air–sea heat flux anomaly into the ocean (left) increased and (center) decreased by 8 W m^{-2} over the subpolar gyre. The surface dynamic height anomaly (contours every 0.2 m; dashed lines are negative) are included to reveal the gyre circulations. (right) Northward heat transport anomalies for positive (red) or negative (blue) anomalies for the upper 100 m for (a) and (b) and for the ocean full depth for (c). Model experiments are performed using MICOM with a monthly cycle in default winds and air–sea fluxes.

boundary, isopycnal depths and salinity are relaxed toward climatology in sponge layers incorporated below the mixed layer. There is an 80-yr spinup of the model forced by climatological monthly winds and air–sea heat fluxes from ECMWF. The model is then integrated for a further 5 yr with perturbed winds or air–sea heat fluxes and compared with the default case; the wind stress is either amplified or dampened by 25% over the entire basin or only over the low latitudes up to 30°N, or the air–sea heat input is enhanced or decreased by 8 W m^{-2} over the subpolar gyre north of 43°N.

a. Wind perturbations

For the wind stress perturbations over the basin, there is enhanced heat content over the subtropics and decreased heat content over the subpolar gyre with enhanced amplitude of wind stress, and the reversed sign of the heat anomaly pattern is found for decreased

amplitude of wind stress (Fig. 10a). This response is the expected effect of enhanced Ekman pumping with stronger winds; greater Ekman downwelling over the subtropics creates a deeper thermocline and increased heat content, and greater Ekman upwelling over the subpolar gyre creates a shallower thermocline and reduced heat content (Fig. 10a). This gyre-scale response is consistent with the sign of the heat content and thermocline anomalies diagnosed for periods when the atmosphere is in an NAO+ state (Fig. 4, left) and opposing signs for an NAO− state (Fig. 4, right).

If the wind stress perturbations are instead confined to the low latitudes up to 30°N, there are still similar signs for the subtropical heat content anomalies, greater subtropical heat content for enhanced trade winds and reduced subtropical heat content for weaker trade winds (Fig. 10b). In both cases of stronger winds, the ocean northward heat transport within the upper 100 m is enhanced from the tropics into the subtropical gyre, while weaker winds lead to the opposing response (Figs. 10a,b).

This model response illustrates how changes in the trade winds induce changes in the subtropical heat content, consistent with our prior diagnostics of how subtropical heat content anomalies are controlled by the northward heat transport driven by low-latitude winds (Figs. 7b,c).

b. Air–sea heat flux perturbations

The effect of air–sea heat fluxes are illustrated for regional heat anomalies over the subpolar gyre. As expected, an air–sea heat flux anomaly directed into the ocean increases the heat content of the subpolar gyre, while an anomaly of opposing sign leads to the opposing response (Fig. 10c). For this case, there is a basin-scale response of the northward heat transport: a warming of the subpolar gyre leads to a reduction in the northward heat transport over the basin, while a cooling of the subpolar gyre leads to the opposing response (Fig. 10c, red and blue lines). Thus, air–sea heat flux forcing leads to a far-field response, involving changes in the meridional overturning circulation, which acts to dampen the original perturbation. The sign of the heat content and heat transport anomalies are consistent with our diagnostics of how the Labrador Sea heat content is negatively correlated with the overturning at 46°N (Fig. 9).

In summary, the idealized model illustrates how subtropical and subpolar heat content anomalies are formed by a combination of wind and air–sea heat flux perturbations; the wind forcing naturally induces gyre contrasts in heat content and the trade winds particularly affect the subtropical heat content, while regional air–sea heat flux anomalies generate local warming and cooling, as well as exciting a larger-scale heat transport anomaly acting to dampen the original perturbation.

6. Discussion

There are significant gyre-scale changes in North Atlantic heat content and thermocline depth on interannual-to-decadal time scales, as well as basin-scale, longer-term trends of warming and deepening of isopycnals. Large-scale changes in atmospheric forcing naturally lead to an opposing sign in the heat anomalies in the subtropical and subpolar gyres: a strengthening in the basin-scale pattern of winds leads to a horizontal Ekman convergence in the subtropical gyre and a divergence in the subpolar gyre; these wind changes automatically deepen and shallow the thermocline over the basin, which in turn increase and decrease heat content respectively. There are also air–sea heat flux changes covarying with these wind speed changes, such as those associated with the North Atlantic Oscillation index (Marshall et al. 2001), acting to enhance the thermal anomalies.

While the atmospheric forcing ultimately induces the gyre contrasts in ocean heat content, the tendencies in ocean heat content are not simply explained by the area-integrated, air–sea heat flux on time scales of typically 5 yr. Instead, the atmospheric forcing is probably important in changing the heat content via changes in the overturning circulation and resulting heat convergence for each gyre.

In the subtropics, variations in the strength of the winds directly alter the Ekman downwelling and depth of the thermocline, as well as leading to concomitant changes in Ekman volume and heat transports at the boundaries. The tendency in heat content over the subtropics is mainly determined by the dynamically controlled heat convergence on time scales of typically 5 yr, as well as possibly augmented by the poorly known air–sea heat fluxes.

In the subpolar gyre, the tendency in heat content over the subpolar gyre does not simply relate either to air–sea heat fluxes or to the Ekman response area averaged over the basin. Instead, the subpolar heat content is altered in a more indirect manner; density changes along the western boundary of the subpolar gyre, probably ultimately induced by atmospheric forcing, are communicated equatorward, altering the overturning and northward heat transport at the intergyre boundary and, in turn, driving changes in the heat convergence over the subpolar gyre. These subpolar heat content and boundary density changes then provide some possible predictability (Robson et al. 2014a; Yeager et al. 2012) through a negative feedback;

when the heat content increases or decreases along the western boundary, ocean dynamics leads to reduced or greater heat convergence within the subpolar gyre, respectively, acting to oppose the original perturbation.

The different mechanisms dominating the heat convergence response for each gyre are probably a fundamental consequence of how heat is transported over the basin. For a climate mean, the northward heat transport is carried by MOC contributions, mainly over the upper 100 m at low latitudes and from 100 to 1300 m at middle-to-high latitudes, and augmented by a gyre contribution at high latitudes (Fig. 6). The winds dominate these low-latitude changes in heat transport by the MOC over the upper 100 m through the Ekman response; for the same wind stress perturbation, the Ekman response is larger in magnitude at low latitudes as a result of the smallness of the Coriolis parameter. The northward heat transport can equivalently be viewed as being carried by a series of contributions: an Ekman cell at low latitudes, a MOC-minus-Ekman cell at middle and high latitudes, and a gyre contribution at high latitudes (Williams et al. 2014). Thus, the sensitivity of the ocean heat content to atmospheric forcing varies within the basin according to how the heat transport and convergence is achieved.

In summary, ocean heat content changes are climatically important and vary in a more complex manner than sea surface temperature through the underlying undulations in thermocline depth. Understanding ocean climate variability via a basinwide response is often misleading, ignoring both wind-induced variations of the thermocline and how overturning changes often differ for each gyre. Understanding the factors controlling the gyre-specific overturning and associated heat convergence is therefore crucial to interpret ongoing North Atlantic climate variability and how the ocean sequesters heat.

Acknowledgments. The authors gratefully acknowledge support from the U.K. Natural Environmental Research Council (ESR10424, NCR10118) and the U.S. National Science Foundation. DS was supported by the U.K. Joint DECC/Defra Met Office Hadley Centre Climate Programme (GA01101). We thank two anonymous referees for constructive comments and Chris Hughes for advice on the Monte Carlo method for identifying significance.

REFERENCES

Bingham, R. J., and C. W. Hughes, 2008: Determining North Atlantic meridional transport variability from pressure on the western boundary: A model investigation. *J. Geophys. Res.*, **113**, C09008, doi:10.1029/2007JC004679.

Bleck, R., and L. Smith, 1990: A wind-driven isopycnic coordinate model of the north and equatorial Atlantic Ocean: 1. Model development and supporting experiments. *J. Geophys. Res.*, **95**, 3273–3285, doi:10.1029/JC095iC03p03273.

Greatbatch, R. J., A. F. Fanning, A. D. Goulding, and S. Levitus, 1991: A diagnosis of interpentadal circulation changes in the North Atlantic. *J. Geophys. Res.*, **96**, 22 009–22 023, doi:10.1029/91JC02423.

Grist, J. P., and Coauthors, 2010: The roles of surface heat flux and ocean heat transport convergence in determining Atlantic Ocean temperature variability. *Ocean Dyn.*, **60**, 771–790, doi:10.1007/s10236-010-0292-4.

Hughes, C. W., and M. Meredith, 2006: Coherent sea-level fluctuations along the global continental slope. *Philos. Trans. Roy. Soc. London*, **364A**, 885–901, doi:10.1098/rsta.2006.1744.

Hurrell, J. W., 1995: Decadal trends in the North Atlantic Oscillation: Regional temperatures and precipitation. *Science*, **269**, 676–679, doi:10.1126/science.269.5224.676.

Josey, S. A., S. Gulev, and L. Yu, 2013: Exchange through the ocean surface. *Ocean Circulation and Climate: A 21st Century Perspective*, 2nd ed. G. Siedler et al., Eds., International Geophysics Series, Vol. 103, Academic Press, 115–140.

Levitus, S., and Coauthors, 2012: World ocean heat content and thermosteric sea level change (0–2000 m), 1955–2010. *Geophys. Res. Lett*, **39**, L10603, doi:10.1029/2012GL051106.

Lozier, M. S., S. Leadbetter, R. G. Williams, V. Roussenov, M. S. C. Reed, and N. J. Moore, 2008: The spatial pattern and mechanisms of heat-content change in the North Atlantic. *Science*, **319**, 800–803, doi:10.1126/science.1146436.

——, V. Roussenov, M. S. C. Reed, and R. G. Williams, 2010: Opposing decadal changes for the North Atlantic meridional overturning circulation. *Nat. Geosci.*, **3**, 728–734, doi:10.1038/ngeo947.

Luyten, J., J. Pedlosky, and H. Stommel, 1983: The ventilated thermocline. *J. Phys. Oceanogr.*, **13**, 292–309, doi:10.1175/1520-0485(1983)013<0292:TVT>2.0.CO;2.

Marotzke, J. R., R. Giering, K. Q. Zhang, D. Stammer, C. Hill, and T. Lee, 1999: Construction of the MIT ocean general circulation model and application to Atlantic heat transport sensitivity. *J. Geophys. Res.*, **104**, 29 529–29 547, doi:10.1029/1999JC900236.

Marshall, J., C. Hill, L. Perelman, and A. Adcroft, 1997: Hydrostatic, quasi-hydrostatic, and nonhydrostatic ocean modeling. *J. Geophys. Res.*, **102**, 5733–5752, doi:10.1029/96JC02776.

——, and Coauthors, 2001: North Atlantic climate variability: Phenomena, impacts and mechanisms. *Int. J. Climatol.*, **21**, 1863–1898, doi:10.1002/joc.693.

Mellor, G. L., C. R. Mechoso, and E. Keto, 1982: A diagnostic calculation of the general circulation of the Atlantic Ocean. *Deep-Sea Res.*, **29A**, 1171–1192, doi:10.1016/0198-0149(82)90088-7.

Pickart, R. S., F. Straneo, and G. W. K. Moore, 2003: Is Labrador Sea Water formed in the Irminger basin? *Deep-Sea Res. I*, **50**, 23–52, doi:10.1016/S0967-0637(02)00134-6.

Robson, J., R. Sutton, K. Lohmann, D. Smith, and M. D. Palmer, 2012: Causes of the rapid warming of the North Atlantic Ocean in the mid-1990s. *J. Climate*, **25**, 4116–4134, doi:10.1175/JCLI-D-11-00443.1.

——, D. Hodson, E. Hawkins, and R. Sutton, 2014a: Atlantic overturning in decline? *Nat. Geosci.*, **7**, 2–3, doi:10.1038/ngeo2050.

——, R. Sutton, and D. Smith, 2014b: Decadal predictions of the cooling and freshening of the North Atlantic in the 1960s and

the role of ocean circulation. *Climate Dyn.*, **42**, 2353–2365, doi:10.1007/s00382-014-2115-7.

Roussenov, V., R. G. Williams, C. W. Hughes, and R. Bingham, 2008: Boundary wave communication of bottom pressure and overturning changes for the North Atlantic. *Geophys. Res. Lett*, **113**, C08042, doi:10.1029/2007JC004501.

Smith, D. M., and J. M. Murphy, 2007: An objective ocean temperature and salinity analysis using covariances from a global climate model. *J. Geophys. Res.*, **112**, C02022, doi:10.1029/2005JC003172.

——, R. Eade, N. J. Dunstone, D. Fereday, J. M. Murphy, H. Pohlmann, and A. A. Scaife, 2010: Skilful multi-year predictions of Atlantic hurricane frequency. *Nat. Geosci.*, **3**, 846–849, doi:10.1038/ngeo1004.

——, and Coauthors, 2015: Earth's energy imbalance since 1960 in observations and CMIP5 models. *Geophys. Res. Lett.*, **42**, 1205–1213, doi:10.1002/2014GL062669.

Straneo, F., 2006: On the connection between dense water formation, overturning, and poleward heat transport in a convective basin. *J. Phys. Oceanogr.*, **36**, 1822–1840, doi:10.1175/JPO2932.1.

Wilks, D. S., 1995: *Statistical Methods in the Atmospheric Sciences.* International Geophysics Series, Vol. 59, Academic Press, 464 pp.

Williams, R. G., V. Roussenov, D. Smith, and M. S. Lozier, 2014: Decadal evolution of ocean thermal anomalies in the North Atlantic: The effects of Ekman, overturning, and horizontal transport. *J. Climate*, **27**, 698–719, doi:10.1175/JCLI-D-12-00234.1.

Yashayaev, I., 2007: Hydrographic changes in the Labrador Sea, 1960–2005. *Prog. Oceanogr.*, **73**, 242–276, doi:10.1016/j.pocean.2007.04.015.

Yeager, S., A. Karspeck, G. Danabasoglu, J. Tribbia, and H. Teng, 2012: A decadal prediction case study: Late twentieth-century North Atlantic Ocean heat content. *J. Climate*, **25**, 5173–5189, doi:10.1175/JCLI-D-11-00595.1.